Supplementary Information: Bayesian analysis of individual electron microscopy images: Towards structures of dynamic and heterogeneous biomolecular assemblies

Pilar Cossio[a,b], Gerhard Hummer[a,b]

[a]*Department of Theoretical Biophysics, Max Planck Institute of Biophysics, 60438 Frankfurt am Main, Germany*
[b]*Laboratory of Chemical Physics, National Institute of Diabetes and Digestive and Kidney Diseases, National Institutes of Health, Bethesda, MD 20892-0520, USA*

1. Supplementary Text

GroEL PDB structures

In Table S1, we list the PDB structures of GroEL used in this study, together with the experimental method, conformational state, and reference. Structures were modified to have the same sequence (by correcting a few minor variations), and the same number of residues (524 for each monomer) as the apo crystal structure with PDB ID 1XCK. For optimal structural alignments, we appropriately permuted the monomer chain identifiers within the two rings. We used the same reference orientation for all structures, with the rotational axis along the z-axis.

To assess the structural similarity between the different models, we list in Table S2 the C_α root mean square deviations (RMSDs) of the entire protein. In Tables S3 and S4, we list the C_α RMSDs between the PDB structures for monomer chains A and H, respectively, as representatives of monomers in the two rings.

In Fig. S1, we plot $\ln(P_{m\omega}/P_{\text{Noise}})$ as a measure of the normalized evidence for model m from image ω, rank-ordered for each model m according to $P_{m\omega}$. Results are shown for models 1KP8, 1PF9, and 1SX4. The models 1XCK, 3C9V and 1AON analyzed in the main text are included with dashed lines for reference. We found similar results as those presented in Fig. 2 of the main text. 1XCK is the most probable structure to have generated the EM

images. Not surprisingly, slightly behind is model 1KP8 that is only 1.7 Å in C_α RMSD from 1XCK. Lowest ranked are structures of GroEL bound to GroES+ADP such as 1PF9 and 1SX4, that are very similar to 1AON (~ 1 Å in C_α RMSD; GroES and nucleotides removed in the calculations).

GroEL symmetry

Fig. S2 shows the log-posterior $\ln(P_{m\omega}/P_{\text{Noise}})$ for models 1XCK and 1AON as a function of the Euler angle α (corresponding to rotations about the z-axis, with $\beta = \gamma = 0$) for a top view image of GroEL (see inset). Points are fitted to $A\sin(f\alpha + c)$. For all models we find a frequency factor of $f = 7$, with α in radians, consistent with the 7-fold symmetry of GroEL. Also, as mentioned in the main text, for this particular image the model 1AON has a higher log-posterior than 1XCK, indicating that top-views are challenging projections for distinguishing overall similar GroEL models.

GroEL coarse-grained model

The GroEL coarse-grained model was constructed with 14 spheres each corresponding to a monomer with 20 Å radius. 7 spheres were centered on the edges of a heptagon with radius 60 Å. The remaining 7 spheres are reflected symmetrically on a plane parallel to the heptagon, with a distance of 80 Å between corresponding centers. In Fig. S3, we plot the coarse-grained model and its dimensions.

Particle classification

As a further test whether we can consistently identify the best structure within a pool of models for a given EM image, we determined the "best" model individually for each of the 1,283 GroEL images. Our model set consisted of the five PDB structures analyzed in Figs. 2-4 of the main text. For each of the 1,283 EM images, we determined the model with the highest log-posterior. In Fig. S4 we plot the relative fraction of GroEL particles for which each PDB model scored at the top. Since we expect images of poor signal-to-noise ratio to have low discriminatory power, we grouped the images according to the top-ranked log-posterior for the five models (less than 250: 471 particles, between 250 and 500: 605 particles, and over 500 relative to noise: 207 particles). As expected, in the group with low posterior, models 1XCK, 3C9V, 2C7E and 1AON perform similarly, each claiming approximately 25 % of the particles. However, for images with intermediate and high probability, model 1XCK performs best, winning out in 60 and 70

% of the images, respectively, over all other models. In the top group, 1XCK and the similar 3C9V structure (RMSD 4.6 Å) jointly claim more than 90 % of all particles.

Similarly, for the ESCRT-I-II system, we find that for the data sets generated from models with extensions $D_{\text{Max}} = 360, 313, 267$, and 227 Å, the percentage of correctly assigned particles is 75, 97.5, 98.5 and 98.5 %, respectively. As mentioned in the main text, the needle-like character of the model with $D_{\text{Max}} = 360$ Å makes it the most challenging structure to distinguish from the 17 other ESCRT models.

Total cumulative evidence versus RMSD

Fig. S5 shows, for all GroEL pdb models, the cumulative evidence $\sum_\omega^\Omega \ln(P_{m\omega}/P_{1XCK,\omega})$ over the whole GroEL image set (Ω) as a function of the C_α RMSDs from structure 1XCK. We find that, overall, the further a structure is (in RMSD) from 1XCK, the lower is its log-posterior, and the less likely it is to have generated the images. We emphasize that we do not expect a perfect correlation since RMSD is only one of many measures of structural differences.

Averaging images leads to loss in discriminatory power

Individual particles within a class unavoidably have small variations in their relative orientations. With our single-image analysis, we can assess the loss of information resulting from averaging over these particles instead of analyzing them individually. Specifically, for model m, we calculated the discriminatory power of the cumulative evidence over the individual particles in a class-set, $\prod_{\omega=1}^{\varpi} P_{m\omega}$, with respect to the posterior over its corresponding class-averaged map, $P_{m\overline{1\ldots\varpi}}$, as a function of the number of averaged images, ϖ, in each set. To represent a class-set, we selected one random orientation of 1XCK, and generated 50 synthetic images that varied with a Gaussian-distributed overall rotational angle of 6 degrees in width from the initial orientation, random noise (signal-to-noise ratio= 0.01 to 0.2), blurring ($\sigma = 1$ to 4Å) and a small center displacement $\pm$ 3Å. To mimic the effect of averaging particles with minute differences in orientation, we averaged over random image pairs, triples, etc. to obtain maps that averaged a different number of the synthetic images. In Fig. S6, we show the average logarithm of the discriminatory power per individual image, for model 3C9V with respect to 1XCK, $\frac{1}{\varpi} \ln(\frac{\prod_{\omega=1}^{\varpi} P_{3C9V,\omega}/P_{3C9V,\overline{1\ldots\varpi}}}{\prod_{\omega=1}^{\varpi} P_{1XCK,\omega}/P_{1XCK,\overline{1\ldots\varpi}}})$, as a function of the number of images

averaged in each class-set. Negative values indicate a loss in log-posterior, per image, for discriminating 1XCK from 3C9V, when averaged class-sets are used instead of individual particles. We find that the information is gradually lost as a function of the number of averaged images. So while averaging within a class improves the SNR (see inset of Fig. S6) the overall information content is nonetheless reduced. This loss of about 15 log units per image as a result of averaging is significant, with the total log-evidence in favor of 1XCK over 3C9V being only $\approx 8000/1283 = 6.2$ per image.

General Point Spread Function

The complex imaging process in cryo-EM is commonly described with a contrast transfer function (CTF) and its real-space equivalent, the point spread function (PSF). The two functions are related through a 2D Fourier transformation,

$$\text{PSF}(r) = \int_0^\infty J_0(rs)\text{Env}(s)\text{CTF}(s)sds \ , \tag{1}$$

where s is the reciprocal radial coordinate, $J_0(rs)$ is the Bessel function of the first kind of order 0 and $\text{Env}(s)$ is the envelope function. The contrast transfer function is commonly approximated as $\text{CTF}(s) = A\cos(as^2/2) - \sqrt{1-A^2}\sin(as^2/2)$ and the envelope function as $\text{Env}(s) = e^{-bs^2/2}$ (Penczek, 2010), with A, a, b parameters. For these functional forms we obtain a simple analytical expression also for the PSF. With $\int_0^\infty J_0(rs)e^{-\gamma^2 s^2/2}sds = \frac{e^{-r^2/2\gamma^2}}{\gamma^2}$, and by using complex arithmetic with $\gamma^2 = b - ia$, the point spread function becomes

$$\text{PSF}(r) = A\text{Re}[\gamma^{-2}e^{-r^2/2\gamma^2}] - \sqrt{1-A^2}\text{Im}[\gamma^{-2}e^{-r^2/2\gamma^2}]$$
$$= \frac{e^{-\chi r^2/2}}{\sqrt{b^2+a^2}}\left(A_R\cos(\theta r^2/2) - \sqrt{1-A_R^2}\sin(\theta r^2/2)\right) \ , \tag{2}$$

where $\theta = a/(b^2+a^2)$, $\chi = b/(b^2+a^2)$ and $A_R = \cos(\cos^{-1}(A) - \tan^{-1}(a/b))$.

In the following, we assess the effect of this general PSF, or equivalently the general CTF, by convolving the PSF with the ideal image $I_0(x', y'|m, \boldsymbol{\varphi})$ (see Main Text Eq. 4),

$$I_{\text{PSF}}(x,y|m,\boldsymbol{\varphi},\chi,\theta,A_R) = \int \text{PSF}(r',\chi,\theta,A_R)I_0(x',y'|m,\boldsymbol{\varphi})dx'dy' \ , \tag{3}$$

4

where $r' = \sqrt{x'^2 + y'^2}$. We also note that for the particular case $\theta = 0$, the PSF$(r) \propto e^{-\chi r^2/2}$ corresponds to the Gaussian blurring described in the Main Text.

We have characterized the performance of the general PSF for a subset of 50 GroEL images. In Fig. S7 A, the cumulative evidence of model 1XCK with the general PSF is compared against 1XCK with only Gaussian blurring, as a function of parameters χ and θ, for $A_R = 1$. We find that the inclusion of the general PSF boosts the posterior of each model with respect to each individual image. Parameters $\chi = 0.00375$ Å^{-2} and $\theta = 0.008$ Å^{-2} maximize the posterior (arrow in Fig. S7 A) by favoring with ~ 3500 log-units the model that includes the general PSF as compared to just Gaussian blurring. In Fig. S7 B, we show the real-space PSF for these parameters, and for the particular case $(\theta = 0, \chi = 1/(8$ Å$)^2)$ corresponding to only Gaussian blurring. To validate this analysis, for each individual image, we calculated the power spectrum of the calculated image (I_{PSF}, see Eq. S3), for parameters that maximized the posterior, $\chi = 0.00375$ Å^{-2}, $\theta = 0.008$ Å^{-2} and $A_R = 1$. In Fig S8 C, we compare the calculated average power spectrum to the corresponding average power spectrum of the experimental GroEL images with background modeled as a Gaussian in s and subtracted (Heymann and Belnap, 2007; Heymann et al., 2008). The curves agree and we thus conclude that including the PSF in the analysis accounts accurately for the contrast transfer effects also in Fourier-space.

Lastly, we assessed the GroEL model ranking when including the PSF in the Bayesian analysis. The posterior probability of the Main Text (see Eq. 3) now includes integrals over (χ, θ, A_R). In Fig. S8, we show the cumulative evidence $\sum_\omega \ln(P_{m\omega})$, of models 3C9V and 3CAU with respect to 1XCK, when parameters χ, θ are sampled within [0,0.0075] Å^{-2}, and [0,0.15] Å^{-2}, respectively, for $A_R = 1$; results with only Gaussian blurring are shown as dashed lines for reference. Tests have also been performed sampling A_R within $[0, 1]$, and the general conclusions remain the same: 1XCK has the highest overall posterior probability, and models 3C9V and 3CAU are ranked slightly lower. Whereas the inclusion of the PSF indeed boosts the posterior for each individual image, the Gaussian blurring is the simplest and most efficient one-parameter representation that accounts well for the major diffraction effects and maintains the correct GroEL model differentiation and ranking. Nonetheless, elaborate CTF models can be handled within our Bayesian approach and further boost the discriminatory power.

5

Overall variations in normalization and offset

Individual EM images vary not only in the molecule conformation and orientation but also the in the detailed imaging conditions. The relative intensities are affected by thermal and mechanical variations, electron dose, ice thickness and proximity to the carbon grid (Penczek, 2010). Moreover, the transformation of the image intensities to zero mean and unit variance affects different projections differently. Introducing additional normalization and offset parameters with respect to the *em2D* score presented in (Velazquez-Muriel et al., 2012), accounts for these overall variations and improves the quality of the posterior without increase in computational expense. To illustrate their importance, we calculated the variations in the posterior probability as a function the offset and normalization for GroEL model 1XCK with respect to two individual experimental images in different projections (top/side view). The results are shown in Fig. S9. Regardless of the fact that both experimental maps are normalized to zero mean and unit standard deviation, we find that the parameter values that maximize the posterior vary significantly from image to image, this depending on the molecule orientation and specific signal-to-noise conditions. Selecting the best parameter values *a priori* is non-trivial, and it would be unlikely to obtain the highest posterior probability for each individual image with a fixed-value set. As a result, to further boost the performance, it is important to account for variations in the offset and normalization, and as shown in the following section, we do so analytically, at no additional computational cost and without numerical integration error.

Analytical integration of the posterior

In the calculation of the Bayesian probability, the posterior is integrated over uniformly distributed parameters of orientation ($\boldsymbol{\varphi}$), blurring (σ), translation ($\mathbf{d}$), normalization (N), offset (μ), and standard deviation of the noise (λ). The Gaussian integrals over N and μ can be evaluated analytically,

$$
\begin{aligned}
P_{m\omega}(\boldsymbol{\varphi}, \sigma, \mathbf{d}, \lambda) &= \\
& \int_{-\infty}^{\infty} \int_{-\infty}^{\infty} \left(2\pi\lambda^2\right)^{-N_{\text{pix}}/2} e^{-\sum_{(x,y)}\left[I_\omega^{(\text{obs})}(x,y) - N I(x,y|m,\boldsymbol{\varphi},\sigma,\mathbf{d}) - \mu\right]^2 / 2\lambda^2} dN d\mu \\
&= \frac{\lambda^{2-N_{\text{pix}}}\left(2\pi\right)^{1-N_{\text{pix}}/2} e^{-\frac{N_{\text{pix}}(C_{cc}C_{oo}-C_{oc}^2) + 2C_o C_{oc}C_c - C_{cc}C_o^2 - C_{oo}C_c^2}{2\lambda^2(N_{\text{pix}}C_{cc}-C_c^2)}}}{\sqrt{N_{\text{pix}}C_{cc} - C_c^2}},
\end{aligned}
\tag{4}
$$

where

$$C_o = \sum_{(x,y)} I_\omega^{(\mathrm{obs})}(x,y) , \tag{5}$$

$$C_c = \sum_{(x,y)} I(x,y|m,\boldsymbol{\varphi},\sigma,\mathbf{d}) , \tag{6}$$

$$C_{oo} = \sum_{(x,y)} [I_\omega^{(\mathrm{obs})}(x,y)]^2 , \tag{7}$$

$$C_{cc} = \sum_{(x,y)} [I(x,y|m,\boldsymbol{\varphi},\sigma,\mathbf{d})]^2 , \tag{8}$$

$$C_{oc} = \sum_{(x,y)} I_\omega^{(\mathrm{obs})}(x,y) I(x,y|m,\boldsymbol{\varphi},\sigma,\mathbf{d}) \tag{9}$$

are the averages and cross-correlations of the intensities of observed (o) and calculated (c) images. A saddle-point-type approximation was used to integrate the posterior over the standard deviation of the noise, λ. We define $f(\lambda) = \ln P_{m\omega}(m,\boldsymbol{\varphi},\sigma,\mathbf{d},\lambda)$. Then, to second order, $f(\lambda) \approx f(\lambda_0) + (\lambda - \lambda_0)^2 \frac{\partial^2 f(\lambda)}{\partial^2 \lambda}|_{\lambda_0}/2$ with λ_0 such that $\frac{\partial f(\lambda)}{\partial \lambda}|_{\lambda_0} = 0$. Under this approximation, the integration of the posterior over λ becomes a Gaussian integral, from which we obtain

$$
\begin{aligned}
P_{m\omega}(\boldsymbol{\varphi},\sigma,\mathbf{d}) \approx {}& \sqrt{\pi}(2\pi e)^{1-N_{\mathrm{pix}}/2} \\
& \times [N_{\mathrm{pix}}(C_{cc}C_{oo} - C_{oc}^2) + 2C_o C_{oc} C_c - C_{cc}C_o^2 - C_{oo}C_c^2]^{3/2-N_{\mathrm{pix}}/2} \\
& \times [(N_{\mathrm{pix}} - 2)(N_{\mathrm{pix}}C_{cc} - C_c^2)]^{N_{\mathrm{pix}}/2-2}.
\end{aligned}
\tag{10}
$$

The remaining integrals over the orientation, blurring, and translation were performed numerically using grid summation.

References

Bartolucci, C., Lamba, D., Grazulis, S., Manakova, E., Heumann, H., 2005. Crystal structure of wild-type chaperonin GroEL. J. Mol. Biol. 354, 940–951.

Chaudhry, C., Farr, G., Todd, M., Rye, H., Brunger, A., Adams, P., Horwich, A., Sigler, P., 2003. Role of the gamma-phosphate of ATP in triggering protein folding by GroEL-GroES: function, structure and energetics. EMBO Journal 22, 4877–4887.

Chaudhry, C., Horwich, A., Brunger, A., Adams, P., 2004. Exploring the structural dynamics of the E-coli chaperonin GroEL using translation-libration-screw crystallographic refinement of intermediate states. J. Mol. Biol. 342, 229–245.

Heymann, J. B., Belnap, D. M., 2007. Bsoft: Image processing and molecular modeling for electron microscopy. J. Struct. Biol. 157, 3–18.

Heymann, J. B., Cardone, G., Winkler, D. C., Steven, A. C., 2008. Computational resources for cryo-electron tomography in Bsoft. J. Struct. Biol. 161 (3), 232–242.

Ludtke, S. J., Baker, M. L., Chen, D.-H., Song, J.-L., Chuang, D. T., Chiu, W., 2008. De novo backbone trace of GroEL from single particle electron cryomicroscopy. Structure 16, 441–448.

Penczek, P. A., 2010. Image restoration in cryo-electron microscopy. Methods in Enzymology 482, 35–72.

Ranson, N., Farr, G., Roseman, A., Gowen, B., Fenton, W., Horwich, A., Saibil, H., 2001. ATP-bound states of GroEL captured by cryo-electron microscopy. Cell 107, 869–879.

Velazquez-Muriel, J., Lasker, K., Russel, D., Phillips, J., Webb, B. M., Schneidman-Duhovny, D., Sali, A., 2012. Assembly of macromolecular complexes by satisfaction of spatial restraints from electron microscopy images. Proc. Natl. Acad. Sci. USA 109, 18821–18826.

Wang, J., Boisvert, D., 2003. Structural basis for GroEL-assisted protein folding from the crystal structure of $(GroEL-KMgATP)_{14}$ at 2.0 Ångstrom resolution. J. Mol. Biol. 327, 843–855.

Xu, Z., Horwich, A., Sigler, P., 1997. The crystal structure of the asymmetric GroEL-GroES-$(ADP)_7$ chaperonin complex. Nature 388, 741–750.
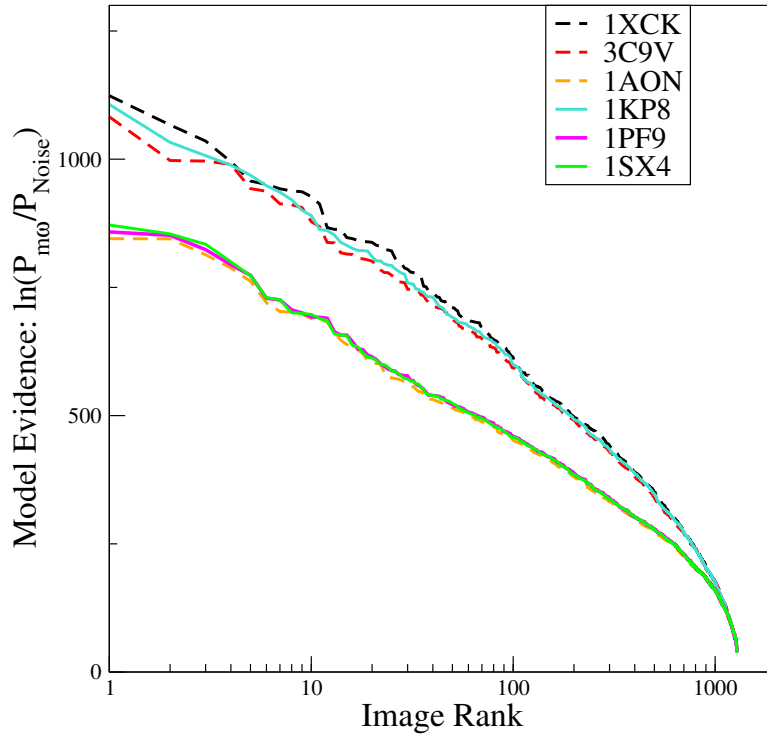
2. Supplementary Figures

Figure S1: **GroEL model discrimination.** Statistical evidence $\ln(P_{m\omega}/P_{\text{Noise}})$ as a function of the rank-ordered experimental image ω for models 1KP8, 1PF9, and 1SX4. The corresponding curves for 1XCK, 3C9V, and 1AON are shown with dashed lines.
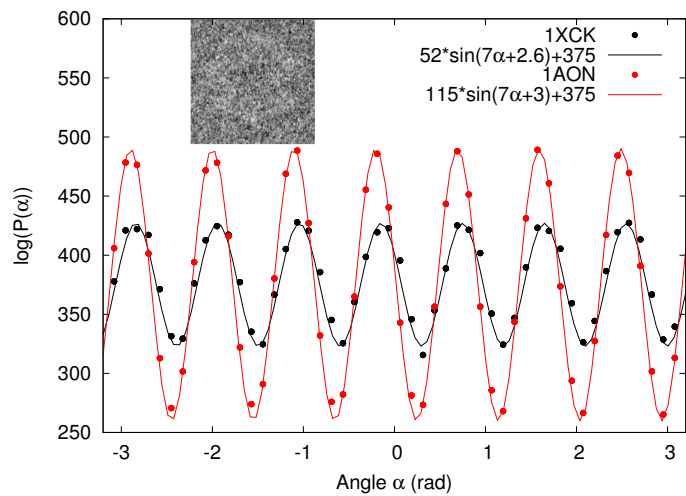
9

Figure S2: **GroEL symmetry assessment.** Statistical evidence $\ln(P_{m\omega}/P_{\text{Noise}})$ as a function of Euler angle α (rotational angle about z-axis) for GroEL models 1XCK (black) and 1AON (red). Euler angles β, γ were set to zero. The inset shows the experimental image (ω), showing GroEL in a top view (shown also in Main text Fig. 1).
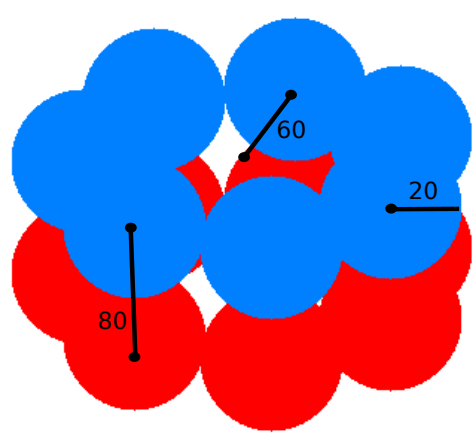

Figure S3: **GroEL Coarse-Grained (CG) model.** Black lines indicate the sphere radius (20 Å), the distance between stacked spheres in the two rings (80 Å), and the distance of the spheres from the symmetry axis (60 Å).
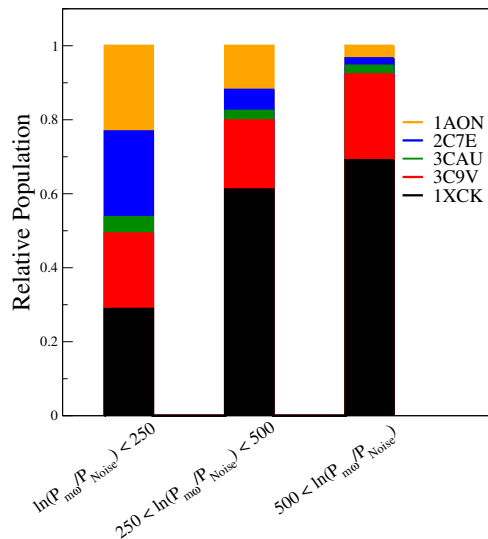
10

Figure S4: **Identifying GroEL models from particles.** Shown is the fraction of GroEL particles for which each model 1XCK, 3C9V, 3CAU, 3C7E, and 1AON has the highest log-posterior. The 1,283 images are grouped according to the log-posterior of the top-performing models, with log-posteriors less than 250, between 250 and 500, and over 500 relative to noise.
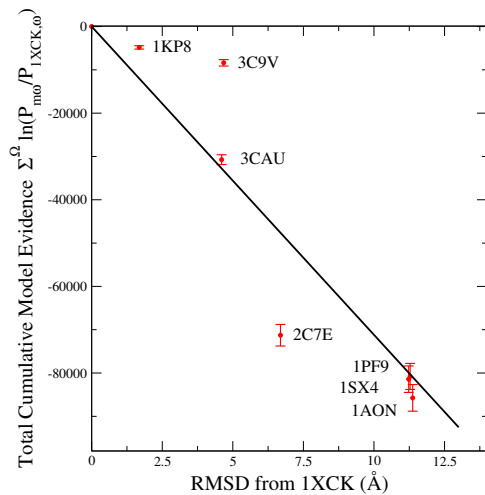

Figure S5: **Cumulative evidence for GroEL models relative to 1XCK versus RMSD.** Shown is the total cumulative model evidence $\sum_{\omega=1}^{\Omega} \ln(P_{m\omega}/P_{1XCK,\omega})$ of model m relative to 1XCK over the whole GroEL image set (Ω) as a function of the C_α RMSD from structure 1XCK, for all GroEL pdb models. Error bars corresponding to one standard deviation were estimated using the bootstrap technique.
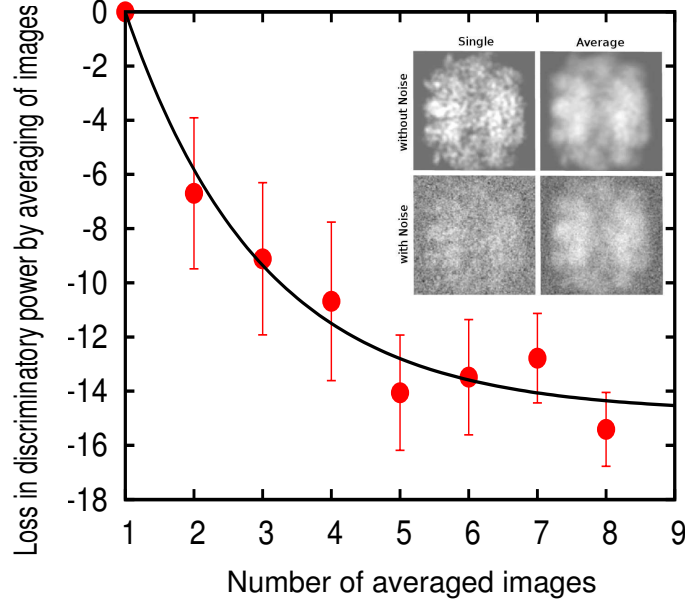
11

Figure S6: **Loss in discriminatory power by averaging images as a result of small variations in the orientation of the particles within a class.** Shown is the average logarithm of the discriminatory power, per individual image for model 3C9V with respect to 1XCK, $\frac{1}{\varpi}\ln\left(\frac{\prod_{\omega=1}^{\varpi}P_{3C9V,\omega}/P_{3C9V,\overline{1\ldots\varpi}}}{\prod_{\omega=1}^{\varpi}P_{1XCK,\omega}/P_{1XCK,\overline{1\ldots\varpi}}}\right)$ as a function of the number of averaged images, ϖ, in a synthetic class-set. Negative values indicate a loss in discriminatory power per image, when averaged class-sets are used instead of individual particles. 50 synthetic images were generated that differ only slightly in the relative orientations of the model 1XCK. Specifically, the model was rotated randomly by an angle with a Gaussian distribution of width 6°, with respect to the reference orientation $\alpha = 110.4°; \beta = 42.1°; \gamma = 151.5°$. Pairs, triples etc. of the resulting images were averaged to create classes. Error bars corresponding to one standard deviation of the mean were estimated using the bootstrap technique. The line is a fit to $c_1(e^{-(x-1)/c_2} - 1)$ as guide to the eye ($c_1 = 14.8, c_2 = 2.1$). Inset: Representative images obtained by averaging 1 (left) and 8 (right) images per class-set, shown with (bottom) and without (top) noise. Averaging improves the SNR (compare bottom left and right images) but sacrifices detail (see top images). This loss in detail is responsible for the lower discriminatory power of the 'class-averaged' images.
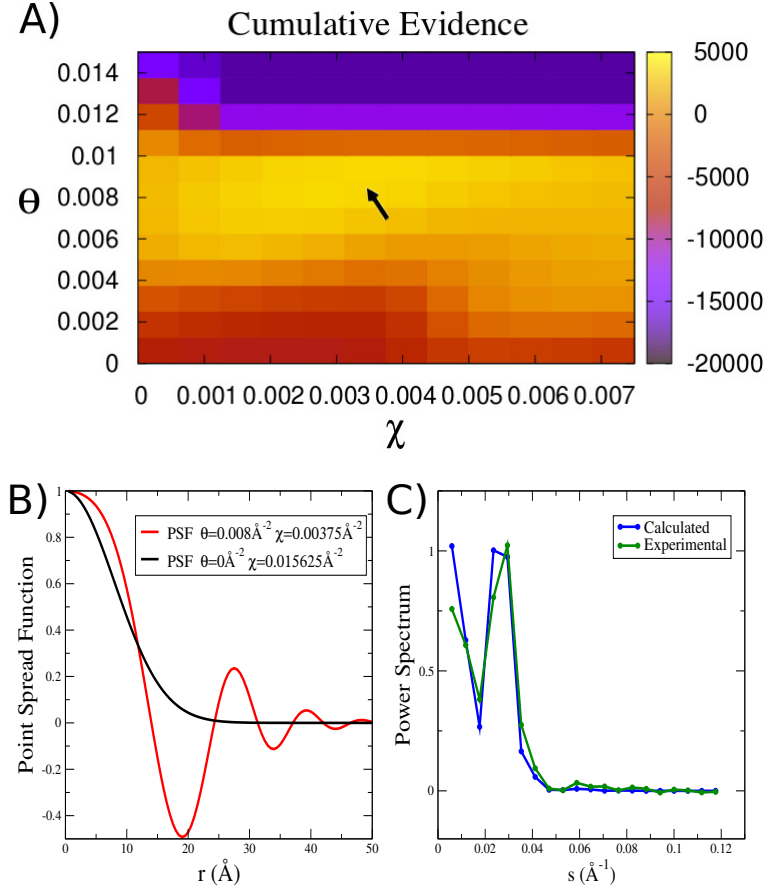
Figure S7: **Effect of general point spread function / contrast transfer function.**
A) Cumulative evidence, $\sum_\omega \ln(P^{PSF}_{m\omega}/P_{m\omega})$, of model 1XCK with PSF against 1XCK
with only Gaussian blurring, as a function of parameters θ, and χ in units of Å^{-2},
for $A_R = 1$, over a sub-set of 50 GroEL experimental images. Remaining parameters
were integrated similarly as in the Main Text: Euler angles α, $\gamma \in (-\pi, \pi)$, $\cos\beta \in$
$(-1, 1)$, $N \in (-\infty, \infty)$, $\mu \in (-\infty, \infty)$, $\lambda \in (0, \infty)$, and $-16 \text{ Å} < d_x, d_y < 16 \text{ Å}$. The
arrow indicates the parameters $\chi = 0.00375 \text{ Å}^{-2}$, and $\theta = 0.008 \text{ Å}^{-2}$ that maximize the
posterior. **B)** Real-space PSF for parameters that maximize the posterior, and for the
case $(\theta = 0, \chi = 1/(8 \text{ Å})^2)$ corresponding to only Gaussian blurring. **C)** Fourier-space
average power spectrum of the experimental GroEL images (Experimental) and of the
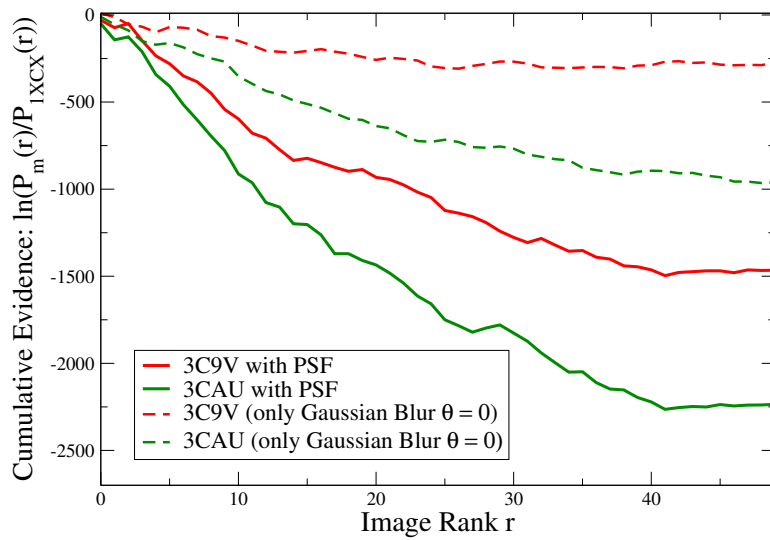back-transformed best I_{PSF} (Calculated).

13

Figure S8: **Bayesian cumulative evidence with the general point spread function.** Shown is the cumulative evidence $\sum \ln(P_m(r)/P_{1\text{XCK}}(r))$ of models 3C9V and 3CAU calculated using the general PSF, as a function of the image rank r for a sub-set of 50 GroEL images. Parameters χ, θ are sampled within $[0, 0.0075]$ Å^{-2}, and $[0, 0.15]$ Å^{-2}, respectively, and $A_R = 1$. Remaining parameters were integrated similarly as in the Main Text. Results with only Gaussian blurring ($\theta = 0$) are included with dashed lines for reference.
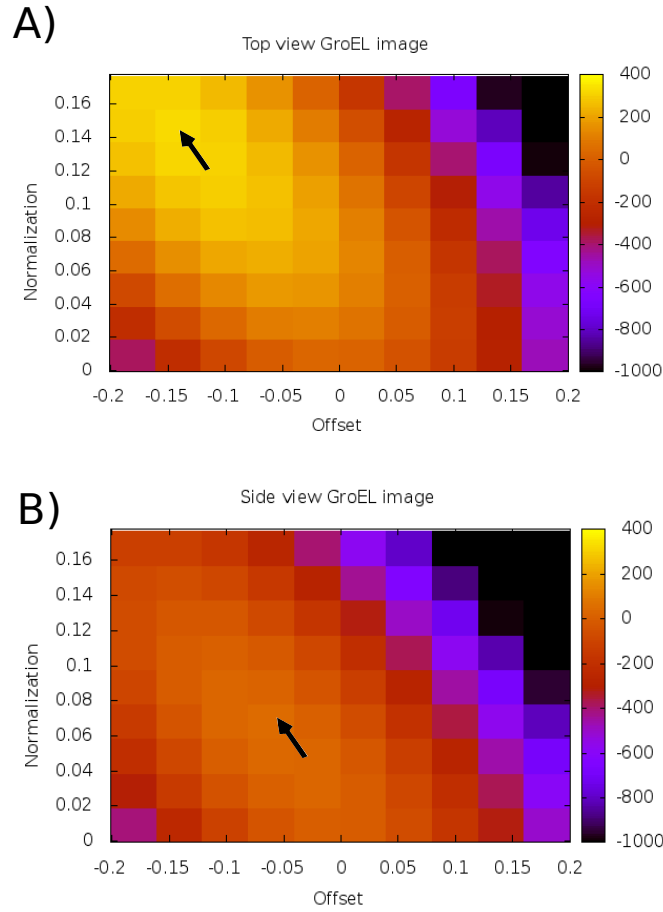
Figure S9: **Effect of variations in offset and normalization.** Shown is the posterior probability of model 1XCK, $\ln(P_{1\text{XCK}}/P_{Noise})$, as a function of offset and normalization parameters, for top (A) and side (B) projections of single-particle GroEL images. Remaining parameters were integrated similarly as in the Main Text. Arrows show the parameter values that maximize the posterior. Note that the optimal values differ in the two projections.

15

3. Supplementary Tables

Table S1: GroEL PDB structures

PDB code	Method	State	Reference
1XCK	X-ray	Apo	(Bartolucci et al., 2005)
1AON	X-ray	GroEL+GroES+ADP	(Xu et al., 1997)
1KP8	X-ray	GroEL+KMgATP	(Wang and Boisvert, 2003)
1PF9	X-ray	GroEL+GroES+ADP	(Chaudhry et al., 2003)
2C7E	EM	GroEL+ATP	(Ranson et al., 2001)
3C9V	EM	Apo	(Ludtke et al., 2008)
3CAU	EM	Apo	(Ludtke et al., 2008)
1SX4	TSL refinement	GroEL+GroES+ADP	(Chaudhry et al., 2004)

Table S2: Full 14-monomer C_α RMSD (Å) between GroEL PDB structures

Model	1XCK	1KP8	3CAU	3C9V	2C7E	1AON	1PF9	1SX4
1XCK	0.000	1.686	4.678	4.604	6.689	11.371	11.281	11.229
1KP8		0.000	4.529	4.509	6.123	11.033	10.941	10.887
3CAU			0.000	2.286	7.025	11.691	11.633	11.584
3C9V				0.000	7.358	11.872	11.811	11.765
2C7E					0.000	10.563	10.486	10.421
1AON						0.000	0.647	0.728
1PF9							0.000	0.342
1SX4								0.000

Table S3: A chain C_α RMSD (Å) between GroEL PDB structures

Model	1XCK	1KP8	3CAU	3C9V	2C7E	1AON	1PF9	1SX4
1XCK	0.000	0.977	4.348	4.329	5.509	12.231	11.999	11.975
1KP8		0.000	4.411	4.390	5.222	11.931	11.694	11.668
3CAU			0.000	2.281	6.520	12.440	12.254	12.230
3C9V				0.000	6.696	12.556	12.364	12.343
2C7E					0.000	12.168	11.935	11.881
1AON						0.000	0.874	0.934
1PF9							0.000	0.356
1SX4								0.000

Table S4: H chain C_α RMSD (Å) between GroEL PDB structures

Model	1XCK	1KP8	3CAU	3C9V	2C7E	1AON	1PF9	1SX4
1XCK	0.000	1.421	4.475	4.487	3.298	1.472	1.515	1.489
1KP8		0.000	4.354	4.340	2.392	1.168	1.175	1.174
3CAU			0.000	2.189	4.769	4.345	4.359	4.347
3C9V				0.000	4.801	4.421	4.439	4.429
2C7E					0.000	2.611	2.594	2.611
1AON						0.000	0.289	0.418
1PF9							0.000	0.284
1SX4								0.000